TECHNICAL NOTE

D-891

LAMINAR HEAT-TRANSFER AND PRESSURE-DISTRIBUTION STUDIES ON A SERIES OF REENTRY NOSE SHAPES AT A MACH NUMBER OF 19.4 IN HELIUM

By Richard D. Wagner, Jr., W. Clint Pine,
and Arthur Henderson, Jr.

Langley Research Center
Langley Field, Va.

NATIONAL AERONAUTICS AND SPACE ADMINISTRATION

WASHINGTON   June 1961

NATIONAL AERONAUTICS AND SPACE ADMINISTRATION

TECHNICAL NOTE D-891

LAMINAR HEAT-TRANSFER AND PRESSURE-DISTRIBUTION STUDIES

ON A SERIES OF REENTRY NOSE SHAPES AT A MACH

NUMBER OF 19.4 IN HELIUM

By Richard D. Wagner, Jr., W. Clint Pine,
and Arthur Henderson, Jr.

SUMMARY

An experimental investigation has been conducted in the 2-inch
helium tunnel at the Langley Research Center at a Mach number of 19.4
to determine the pressure distributions and heat-transfer characteristics
of a family of reentry nose shapes. The pressure and heat-transfer-rate
distributions on the nose shapes are compared with theoretical predictions
to ascertain the limitations and validity of the theories at hypersonic
speeds. The experimental results were found to be adequately predicted
by existing theories. Two of the nose shapes were tested with variable-
length flow-separation spikes. The results obtained by previous investi-
gators of spike-nose bodies were found to prevail at the higher Mach
number of the present investigation.

INTRODUCTION

In recent years considerable effort has been expended on the study
of the aerodynamics and heat-transfer characteristics of blunt-nose
shapes at supersonic and low hypersonic speeds. The variety of nose
shapes tested has made possible an assessment of the limitations and
validity of theoretical predictions of the pressure distributions and
heat-transfer characteristics of general blunt-nose shapes at these
speeds. Present aerodynamic research of this nature, in keeping pace
with requirements, is extending knowledge to ever increasing flight
speeds. Inasmuch as there is only limited available information on the
pressure distributions and heat-transfer characteristics of general
blunt-nose shapes at hypersonic speeds in the reentry Mach number range,
a proper assessment of these quantities and of the validity and limita-
tions of theoretical predictions in this flight regime is still in
progress.

The efforts previously expended to the study of blunt-nose shapes were initiated by the results obtained in reference 1. Here it was shown that the blunt-nose shape has the advantage of alleviating the heating problem associated with the reentry of ballistic missiles. However, associated with the high-drag blunt-nose shape, are subsonic impact velocities which render a missile more vulnerable to detection and interception. For this reason, among others, it is desirable to devise a configuration that would have as low drag as possible consistent with tolerable heat-transfer characteristics. For several years it has been known that the drag of a blunt body at supersonic speed can be greatly reduced through the use of flow-separation spikes ahead of the body (refs. 2 to 5). In an investigation of the flow over a spike-nose hemisphere-cylinder at a Mach number of 6.8 (ref. 2), it was found that the pressure drag coefficient was reduced by all spike lengths studied and, in addition, it was found that the integrated convective heat transfer was decreased about 50 percent by the addition of a spike when laminar flow existed on the separated boundary. Where transition occurred on the separated boundary the integrated convective heat transfer was nearly twice the no-spike value. It has been observed, however, that the stability of the separated laminar layer increases considerably with increasing Mach number, from subsonic Mach numbers to Mach numbers near 6 (refs. 2 and 6). In reference 2 it is observed that at Mach numbers near 6.0 the transition Reynolds numbers for the separated boundary appear to be approaching those for a flat plate. Extrapolation of these results would indicate that at hypersonic speeds where laminar flow is expected to prevail, the use of flow-separation spikes would give the previously mentioned desired lower drag and heating. The results of reference 5 obtained in helium at a Mach number of 14 are indicative of the preceding comments.

Inasmuch as there is only limited available information at the present time on the pressure distributions and heat-transfer characteristics of general blunt-nose shapes, with or without flow-separation spikes, in the reentry Mach number range, an investigation has been conducted in the 2-inch helium tunnel at the Langley Research Center to determine the heat-transfer characteristics and pressure distributions of a family of reentry nose shapes and the effects of flow-separation spikes ahead of blunt-nose shapes. All tests in this investigation were conducted at a Mach number of 19.4 which is well within the reentry Mach number range. It should be noted that true simulation of reentry conditions are not obtained in that the test medium, helium, has different thermodynamic properties than air and is devoid of the effects of dissociation and ionization. However, it has been shown in reference 7 that pressure distributions, at least on blunt noses, are essentially unaffected by the state of the gas; several authors have indicated that the same may also be true for heat-transfer distributions. (See, for instance, ref. 8.)

L
1
3
4
5

SYMBOLS

A	coefficient in equation of meridian curve of nose shapes
b	distance along the nose surface from stagnation point to nose-cylinder junction
$C_{D,p}$	pressure drag coefficient
c_p	specific heat, at constant pressure
c_w	heat capacity of model material
d	base diameter of model
h	film coefficient of heat transfer defined as $\dfrac{q_w}{T_{aw} - T_w}$
h_o	film coefficient of heat transfer at stagnation point
l	spike length
l_n	nose length
M	Mach number
n	exponent in equation of meridian curve of nose shapes
p	local pressure
N_{Pr}	Prandtl number $\left(N_{Pr} = 0.68 \text{ for helium}\right)$
q	local heat-transfer rate per unit area
q_o	local heat-transfer rate per unit area at the stagnation point
R	local radius of curvature
r	local body radius, see figure 2
R_d	Reynolds number based on model diameter
s	distance along surface of model measured from stagnation point
T	temperature

t	time
u	local velocity
x	Cartesian coordinate
β	curvature correction factor
γ	ratio of specific heats ($\gamma = 5/3$ for helium)
δ	angle between model center line and a tangent to surface meridian curve
θ_c	equivalent cone angle
μ	coefficient of viscosity
ρ	density
ρ_w	density of model material
τ	wall thickness
ω	power in viscosity power law ($\omega = 0.647$ for helium)

Subscripts:

h	evaluated at the stagnation point on the hemisphere
w	wall conditions
aw	adiabatic wall condition
t_1	free-stream stagnation conditions
t_2	stagnation conditions behind normal shock at free-stream Mach number
1	free-stream static conditions

L
1
3
4
5

APPARATUS AND PROCEDURE

Tunnel

The present experimental investigation was conducted in the 2-inch helium tunnel at the Langley Research Center described in references 9 and 10. A schematic diagram of the tunnel and the test apparatus is shown in figure 1. Helium was supplied from a 67-cubic-foot reservoir and passed through a heat exchanger to the stagnation chamber. The stagnation pressure is regulated by an adjustable pressure regulating valve with a maximum obtainable stagnation pressure of 3,000 lb/sq in. gage. With the heat exchanger it is possible to obtain a stagnation temperature of approximately 690° R.

All tests were made in the schlieren test section which employs a 0.052-inch-diameter throat followed by a conical nozzle which expands with a semidivergence angle of 5° from the throat to a constant 2-inch-diameter section. Models were located in the tunnel at a station corresponding to a free-stream Mach number of 19.4 as determined by the calibration in reference 9 and corrected as indicated in reference 11. The effect of the axial Mach number gradient in the tunnel was considered negligible for the model fineness ratios of the present tests. (See ref. 7.)

Models

In this investigation three sets of models of a family of reentry nose shapes and a hemisphere-cylinder were tested. Drawings of the models are shown in figure 2 with the locations of pressure orifices and thermocouples. The equation of the generating curve of the family of nose shapes is:

$$x = Ar^n$$

where x and r are rectangular Cartesian coordinates (see fig. 2), and A and n are constants. The values of n are 1, 2, 4, 6, and 8. The value of A was determined by fixing the fineness ratio of the nose shapes at 1. The nose shapes were attached to cylindrical afterbodies with a diameter of 0.375 inch. A drawing showing construction details typical of the three sets of models is shown in figure 3.

The first set of models were instrumented with 0.020-inch-diameter pressure orifices at the locations indicated in figure 2. The orifices were spiraled around the model at 45° intervals to facilitate installation.

The models were constructed of Inconel and had a 0.030-inch wall thickness. When necessary for obtaining data and for tunnel starting purposes, the blunt shapes were equipped with retractable center-line spikes.

The second set of models were identical with the first set except that they were instrumented with No. 30 gage iron-constantan thermocouples (0.010-inch-diameter wire) and were equipped with cooling tubes, inside the models, which were connected to a bottle of pressurized carbon dioxide. The thermocouples were distributed in the model in the same locations as the pressure orifices and were silver soldered in place so that the effective junction was at the inner face of the model wall. Extreme care was taken in the construction of these models to assure a uniform wall thickness of 0.030 inch.

The third set of models were also instrumented with thermocouples. These models were constructed by electroplating nickel on a mandrel and machining the plating to the desired outside dimensions. The afterbody was tapered 0.25° to assure easy removal of the model from the mandrel. The thickness of the walls of the models was measured at the thermocouple locations and was found to be approximately uniform at 0.010 inch. Chromel-alumel thermocouples of No. 36 gage wire (0.005-inch-diameter wire) were used to instrument the model. The method of installation was the same as that used on the thicker wall models. Due to the frailness of this thermocouple wire the models required more support structure than the 0.030-inch wall models as can be seen in figure 3. Duplicate models of the n = 2 model (a parabolic nose shape) and the hemisphere-cylinder were made, one having a center-line variable spike and the other a stagnation point thermocouple. The other models of this set did not have center-line spikes but instead had stagnation point thermocouples.

INSTRUMENTATION AND ACCURACY

Pressure Measurement

Stagnation pressures in the settling chamber were measured on a Bourdon gage with an accuracy of ±5 lb/sq in. Static pressures on the models were read on mercury manometers and butyl phthalate manometers. Pressures reading less than 0.5 inch of mercury were read on the butyl phthalate manometer. The reference pressure on the mercury and butyl phthalate manometers was maintained at less than 20 microns of mercury. The estimated accuracy of the measured static pressures was ±0.01 lb/sq in. on the mercury manometer and ±0.0007 lb/sq in. on the butyl phthalate manometer.

Temperature Measurement

The stagnation temperature in the settling chamber was measured on an oscillograph which recorded the output of a No. 30 gage iron-constantan thermocouple located in the settling chamber. The temperature-time histories of the heat-transfer models were obtained from thermocouples, located in the model, whose outputs were registered on a multichannel oscillograph.

TEST CONDITIONS AND PROCEDURE

Pressure-Distribution Test

For all tests the models were located in the tunnel at a station corresponding to a free-stream Mach number of 19.4 and were alined along the tunnel center line at zero angle of attack and zero angle of yaw. For the pressure tests the supply helium bypassed the heat exchanger. The stagnation temperature was constant for any given test and always in the range from 539° R to 552° R. The stagnation pressure in the settling chamber, for all tests, was maintained at a constant value of 2,000 lb/sq in. gage by an adjustable pressure regulating valve. These test conditions gave a Reynolds number based on body diameter of 0.30×10^6.

Prior to testing, the models were thoroughly outgassed because of the low pressures encountered. (The importance of outgassing effects at low pressures is discussed in ref. 7.) During the tests the surface static pressures registering on the manometers were photographically recorded at the steady-state condition, which usually was obtained after 90 to 120 seconds of running time.

Heat-Transfer Tests

In obtaining heat-transfer data on test models several conditions must be met by the test procedure. A sufficient step input of temperature must be supplied to give measurable heat-transfer rates. Also, if adequate means of evaluating conduction effects in the model are not available, valid data is available only in the initial phase of the test where the temperature distribution over the model surface is essentially isothermal. This means that the tunnel starting transients must be either eliminated or minimized such as to obtain an interval in the initial phase of the test where the starting transients and conduction effects are negligible.

L
1
3
4
5

In order to obtain a satisfactory step input in temperature to measure transient heating, the supply helium was passed through a heat exchanger prior to entering the settling chamber, and the models were cooled prior to testing by cooling tubes which released pressurized carbon dioxide inside the models. In this manner it was possible to obtain a temperature difference of approximately 200° to 250° R between the test model and the heated supply helium.

The problem of minimizing starting transients was complicated by the fact that the bluntness of the model to be tested was critical in determining whether the flow could be established without the use of an external starting device. Consequently two test procedures were adapted, one to obtain data on the models which presented no difficulties in establishing flow and one for those models requiring external starting devices.

L
1
3
4
5

The models requiring no external starting devices were tested using the procedure described in reference 10. A copper plug placed in the tunnel throat was used to isolate the stagnation chamber and the test section. The model was cooled with the carbon dioxide coolant, and after the coolant was turned off and the stagnation chamber filled with helium at 2,000 lb/sq in. gage, the throat plug was rapidly removed and flow established. The capacity of the helium supply was sufficient to have only an approximate 2-percent decrease in the stagnation pressure during a 10-second test. The initial expansion through the throat caused a slight but negligible decrease in the stagnation temperature.

In order to test models requiring an external starting device a Micarta sleeve was constructed which slid over the model and was connected by wires to a quick acting pneumatic cylinder external to the tunnel. Four 0.030-inch-diameter flexible wires were mounted on the sleeve and formed an effective conical nose on the front of the sleeve which allowed the flow to start with the sleeve on the model. The end of the sleeve open to the flow was covered by a paper disk. A drawing showing the construction of the sleeve and its mounting on the model is shown in figure 4. The testing procedure employing the Micarta sleeve was as follows. The model with the sleeve on was first cooled by the carbon-dioxide coolant. When the model was sufficiently cool, the carbon dioxide was turned off, and the tunnel started. The Micarta sleeve achieved almost perfect insulation between the model and the stream as steady test conditions were established in the tunnel. When steady flow conditions were established, the pneumatic cylinder was actuated which slid the sleeve off the model and the model tore through the paper disk.

Typical temperature-time histories for the two test procedures are presented in figure 5. The duration and magnitude of the transient effects appear to be negligible for both procedures. Thus, for any given heat-transfer test, the stagnation temperature was essentially

constant and always in the range from 668° R to 697° R. With a stagnation pressure of 2,000 lb/sq in. gage and a free-stream Mach number of 19.4, these test conditions gave a Reynolds number based on body diameter of 0.23 × 10⁶.

Heat-Transfer-Data Reduction

The aerodynamic heat-transfer rates were calculated from temperature-time histories during the transient heating of the models at the earliest possible time when starting transients and conduction effects were believed to be negligible. In all cases this required only the use of the first 0.30 second of data. During this time temperatures were recorded at 0.01-second intervals for each thermocouple in the model, and the slopes of faired temperature-time histories were obtained at the earliest possible time for negligible starting transients which never exceeded 0.02 second. At this early time the model was still essentially isothermal, and conduction along the surface was believed to be negligible. The errors associated with the time for heat diffusion normal to the wall as well as heat conduction along the thermocouple wire were assumed to be negligible but will be discussed later. The temperature-time histories indicated negligible radiation losses. With the previously mentioned terms negligible, the aerodynamic heat transfer may be equated to the heat absorbed by the model skin per unit of time. This relation is expressed in the following equation:

$$q = \rho_w c_w \tau \frac{dT_w}{dt} \beta \qquad (1)$$

where the curvature correction factor is given in reference 12 as

$$\beta = \left(1 - \frac{\tau}{2r} \cos \delta\right)\left(1 - \frac{\tau}{2R}\right) \qquad (2)$$

The aerodynamic heat-transfer rate was evaluated by using the mass density ρ_w and specific heat c_w of Inconel and nickel as given in references 13 and 14 and by measuring wall thicknesses. When knowledge of the inviscid flow about the model permitted, the experimental pressures and a recovery factor equal to the square root of the Prandtl number were used to determine the adiabatic wall temperature. The film coefficient

of aerodynamic heat transfer h was then found from the relation

$$h = q(T_{aw} - T_W) \qquad (3)$$

In reference to figure 5, clearly the accuracy of the data is
dependent upon the magnitude of the local heat-transfer rate. Where
sizable heat-transfer rates occur on the model surface, the slope of
the temperature-time histories can be accurately obtained; however,
this accuracy falls off as the heat-transfer rate decreases. Since the
data were obtained when starting transients and lateral conduction effects
were negligible, a further question which may arouse doubt as to the
accuracy of the data would be the unknown possible errors associated
with the wall thickness and heat losses to the thermocouple wire. This
question initiated the construction and tests of the third set of models.
The repeatability of the data obtained on the models of different skin
thickness and different diameter thermocouple wire should be indicative
of any effects of the aforementioned possible errors. For sizable
heating rates the repeatability of the data is good, but for relatively
low heating rates the repeatability begins to falter. However, this
may be due not to these errors but to the previously mentioned inaccu-
racy in obtaining the slopes of temperature-time histories for low
local heating rates.

<div align="right">
L
1
3
4
5
</div>

RESULTS AND DISCUSSION

Schlieren Photographs

Schlieren photographs taken during the tests are shown in figure 6.
In all tests of models without spikes, except the n = 1 model which
is a 26.62° half-angle cone, the models had a detached bow shock wave.
(See fig. 6(a).) Photographs of the n = 2 model and the hemisphere-
cylinder equipped with flow-separation spikes of various lengths are
shown in figures 6(b) and 6(c), respectively. The detached shock obtained
without a spike is seen to be replaced by a conical shock up to the
impingement point of the shock on the body. For the longer spike lengths
this conical shock seems to envelop the model. The addition of the spike
appears to create a disturbance which may be interpreted as an extremely
thick boundary layer on the afterbodies.

Theoretical Methods of Pressure Prediction

The theoretical pressure distribution on the nose portion of the
n = 1 model was calculated by using conical flow theory which gives a

uniform pressure over the surface. To obtain the pressure on the cylindrical afterbody, a Prandtl-Meyer expansion at the nose-cylinder junction was assumed with no pressure decay with distance from the junction.

To obtain theoretical pressure distributions on the nose portion of the models having detached bow waves, the method of incorporating the modified Newtonian theory matched with the Prandtl-Meyer expansion near the nose-cylinder junction was used. (See ref. 15.) The modified blast-wave theory of reference 16 with the pressure at the nose-cylinder junction as given in reference 17 was used to calculate the pressure distributions on the cylindrical afterbodies.

Theoretical and Experimental Pressure Distributions

In figure 7 are shown the theoretical and experimental pressure distributions for the models without flow-separation spikes. For the $n = 1$ model the theoretical prediction of conical flow theory shows excellent agreement with the data over the cone surface. However, on the cylindrical afterbody the pressures are considerably greater than that predicted by a Prandtl-Meyer expansion at the nose-cylinder junction. The viscous nature of the flow in this region which is not accounted for by the Prandtl-Meyer theory may be the reason for this discrepancy, for example, the possible effects of a pressure bleedoff through the boundary layer at the nose-cylinder junction.

In general, the data obtained on the blunt-nose shapes show good agreement with the theoretical predictions. The discrepancies between data and theory near the nose-cylinder junction may again be attributed to pressure bleedoffs through the boundary layer at the nose-cylinder junction. The data are indicative of this since better agreement is obtained on the blunter nose shapes which have the smaller turning angles at the nose-cylinder junction. (See fig. 2.)

The measured pressures on the cylindrical afterbodies show fair agreement with the modified-blast-wave theory with the exception of the hemisphere-cylinder. In references 16 and 18 it is shown that when experimentally determined viscous effects are incorporated in the modified-blast-wave theory good agreement is obtained for the hemisphere-cylinder. It should also be noted that the measured pressures on the afterbody show a more rapid decay of pressure with distance from the shoulder for lower nose drag; this is in accordance with the unmodified-blast-wave theory.

The pressure distributions on the $n = 2$ model and the hemisphere-cylinder equipped with flow-separation spikes of various lengths are shown in figure 8. The effect of the spike is to reduce the overall

pressure level over the nose for all the spike lengths tested. For both models the effect of increasing the spike length is a progressively larger reduction in the pressure level up to an l/d of approximately 3. For larger values of l/d this effect lessens, and little change in the pressure level is accomplished by lengthening the spike. The peak in the pressure level on both nose shapes occurs most upstream on the nose for an l/d of 0.5, and for larger values of l/d it appears somewhat stationary.

The effect of the spike on the afterbody is only slight. Notice, however, on the $n = 2$ afterbody it appears that at any given station there is a reversal in the effect of the spike length. The measured pressures show a decreasing then an increasing pressure with increasing l/d. This may be due to the shock impingement point on the body moving aft with increasing l/d. This effect is not found on the hemisphere-cylinder afterbody; the addition of the spike lowers the pressure level, but there is no apparent effect due to spike length.

For the models tested with flow-separation spikes approximate pressure drag coefficients were calculated by integrating the measured pressure distributions over the noses. These pressure drag coefficients are shown in figure 9. The approximate pressure drag coefficients for $l/d = 0$ are in good agreement with the Newtonian prediction. (Note that the term approximate is used since the integrated pressure distributions were assumed point-to-point straight lines through the sparse number of data points on the noses.) For both nose shapes the pressure drag coefficient rapidly decreases for increasing l/d up to an $l/d = 3.0$ and then levels off. This would be expected from the pressure distributions. Note also that the $n = 2$ model gives lower pressure drag than the hemisphere-cylinder for any given spike length.

The experimental pressure drag coefficients are compared with what may be termed an equivalent cone theory suggested by the existence of the conical shock wave formed by the spike. The equivalent cone theory assumes the spike forms an effective cone with the cone semiangle for the $n = 2$ model which is given by

$$\theta_c = \cot^{-1} \frac{2\left(l + l_n\right)}{d} \tag{4}$$

and for the hemisphere-cylinder

$$\theta_c = \sin^{-1}\left(\frac{1}{1 + \dfrac{2l}{d}}\right) \tag{5}$$

The pressure drag coefficients of these effective cones were then calculated by conical flow theory. The forms of equations (4) and (5) were suggested by the schlieren observations. (See fig. 6.) Equation (4) is the cone angle of a cone with vertex at the tip of the spike and base at the nose-cylinder junction. For the hemisphere the equivalent cone angle given by equation (5) is the half-angle of a cone with vertex at the tip of the spike and tangent to the hemisphere surface. In addition the pressure drag coefficients of equivalent cones based on measured shock angles were also calculated.

For the $n = 2$ model the equivalent cone rule using either equation (4) or the measured shock angles is seen in figure 9 to be a good approximation of the data. However, the equivalent cone rule using equation (5) or measured shock angles underpredicts the hemisphere data although good agreement is shown between the measured shock angles and equation (5). Obviously the use of equation (4) for the hemisphere would only give poorer agreement.

Shown also in figure 9(b) are the results of references 2 and 5 for a separated laminar layer. Good agreement is shown between the present results and the results of these investigators.

Theoretical Methods of Heat-Transfer Prediction

At present several methods are available for the prediction of the laminar heat transfer around a given nose shape. (See refs. 19 to 21.) However, due to its amenity for hand calculation, the method presented by Lees in reference 19 was employed with a modification included to account for finite wall temperatures and the variation of the product of the density and viscosity.

For the case of a highly cooled wall, Lees reasoned that the effect of the pressure gradient on the enthalpy gradients at the surface of a body was small, and the enthalpy gradient at the wall is represented quite accurately by the zero pressure-gradient value. To partially account for wall conditions that are not so highly cooled this enthalpy gradient is here taken as $0.5 N_{Pr}^{1/3}(T_{aw} - T_w)/T_t$. With this assumption the film coefficient of heat transfer at the wall is (with N_{Pr} a constant)

$$h = 0.5 N_{Pr}^{-2/3} \frac{\mu_w \rho_w u r c_p}{\left[2(\rho\mu)_{t2} u_1 \int_0^s \frac{\rho\mu}{(\rho\mu)_{t2}} \frac{u}{u_1} r^2 ds \right]^{1/2}} \tag{6}$$

At the stagnation point equation (6) reduces to

$$h_0 = 0.5 \sqrt{2} \; N_{Pr}^{-2/3} \sqrt{(\rho\mu)_{t2}} \sqrt{u_1} \; c_p \; \frac{(\rho_w\mu_w)_{s=0}}{(\rho\mu)_{t2}} \sqrt{\frac{1}{u_1}\left(\frac{du}{ds}\right)_{s=0}} \tag{7}$$

The ratio of the local surface heat-transfer coefficient to the stagnation-point heat-transfer coefficient can now be written as,

$$\frac{h}{h_0} = \frac{0.5 \frac{u}{u_1} \frac{\rho_w\mu_w}{(\rho_w\mu_w)_{s=0}} r}{\left[\int_0^s \frac{\rho\mu}{(\rho\mu)_{t2}} \frac{u}{u_1} r^2 ds\right]^{1/2} \sqrt{\frac{1}{u_1}\left(\frac{du}{ds}\right)_{s=0}}} \tag{8}$$

For an isothermal wall and a perfect gas

$$\frac{\rho_w\mu_w}{(\rho_w\mu_w)_{s=0}} = \frac{p}{p_{t2}} \tag{9}$$

hence

$$\frac{h}{h_0} = \frac{0.5 \frac{u}{u_1} \frac{p}{p_{t2}} r}{\left[\int_0^s \frac{\rho\mu}{(\rho\mu)_{t2}} \frac{u}{u_1} r^2 ds\right]^{1/2} \sqrt{\frac{1}{u_1}\left(\frac{du}{ds}\right)_{s=0}}} \tag{10}$$

Assuming the viscosity power law $\left(\mu \propto T^\omega\right)$ for hypersonic flow, equation (10) becomes

$$\frac{h}{h_0} = \frac{0.5\left(\frac{p}{p_{t2}}\right)\sqrt{1 - \left(\frac{p}{p_{t2}}\right)^{\frac{\gamma-1}{\gamma}}} r}{\left[\int_0^s \left(\frac{p}{p_{t2}}\right)^{\frac{\omega\gamma+(1-\omega)}{\gamma}} \sqrt{1 - \left(\frac{p}{p_{t2}}\right)^{\frac{\gamma-1}{\gamma}}} r^2 ds\right]^{1/2} \sqrt{\frac{1}{u_1}\left(\frac{du}{ds}\right)_{s=0}}} \tag{11}$$

Lees' equation is obtained by taking $\omega = 1$ (in eq. (11)), effectively assuming the product $\rho\mu$ to be constant.

For a given nose shape and pressure distribution, equation (11) can be graphically solved for given test conditions provided the stagnation-point-velocity gradient can be determined. At present there is no method available, other than numerical methods, to calculate the exact stagnation-point-velocity gradient on a blunt-nose shape. However the Newtonian stagnation-point-velocity gradient is known to give a very good approximation for a hemisphere. This being the case the heat-transfer distributions on the nose shapes were calculated in the form of the ratio of the local film coefficient to the stagnation-point film coefficient on a hemisphere-cylinder by using equation (11) with $(du/ds)_{s=0}$ taken as the Newtonian value for a hemisphere with the same base radius as the test models. Experimental pressure distributions were used in these calculations. The sparsity of the experimental pressure-distribution data prevented the calculation of the heat-transfer distribution in the stagnation region.

Theoretical and Experimental Heat-Transfer Distributions

In figure 10 are shown the theoretical and experimental heat-transfer distributions of the six nose shapes investigated. The data are presented with the measured stagnation-point film coefficient on the hemisphere-cylinder as datum. In handling the models, some thermocouples were unavoidably damaged, and consequently data were not obtained at their locations in the model. With the exception of comparisons with spike-nose data, the data on the cylindrical afterbodies are not presented since temperature-time histories in this region indicated essentially zero aerodynamic heat transfer, and the accuracy of the data was at its worst. In general, however, the repeatability of the two sets of data on the nose portions of the models is considered to be good.

On the $n = 1$ (26.62° cone) nose shape, the modified Lees' theory ($\rho\mu$ is a variable) shows good agreement with the data. Lees' original theory overpredicts the data by approximately 30 percent. In addition to the aforementioned methods of calculating the heat-transfer distribution, the T-prime method modified by the Mangler transformation and the modified Reynolds analogy was used to calculate the heat-transfer distribution on the $n = 1$ nose shapes. For the present test conditions this method gave essentially the same results as the modified Lees' method and is therefore not shown.

The agreement between the data and theory is in general good for the blunt-nose shapes. It can be seen that for these cases the modification of Lees' theory gives only slightly different results which are lower than the original prediction. Both predictions fall within the

experimental accuracy of the data. Unfortunately, the 0.010-inch-wall
n = 8 model was damaged prior to testing and the data were not available
to serve as a check of the data obtained on the 0.030-inch-wall model.

The stagnation-point heat-transfer rate on the n = 4 model does
not conform with the Newtonian prediction which gives the stagnation-
point heating to be inversely proportional to the square root of the
nose radius of curvature. The Newtonian prediction would indicate a
lower heat-transfer coefficient on the n = 4 model than that on a
hemisphere.

In figure 11 is shown the heat-transfer distributions obtained on
the models equipped with flow-separation spikes. The film coefficient
of heat transfer was not used in presenting the data since a sufficient
knowledge of the external inviscid flow was not available to determine
the adiabatic wall temperatures. Instead the data are presented as the
ratios of the local measured heat-transfer rates to the stagnation-point
heat-transfer rate of the hemisphere-cylinder. The stagnation-point
heat-transfer rate was obtained by using the measured film coefficient
of heat transfer on the hemisphere-cylinder and the appropriate wall
temperature. The scatter in the data may be attributed to the inaccuracy
of the data since the accuracy was at its worst condition because of the
extremely low heating rates.

For the n = 2 model, the addition of the spike lowers the heating
rates over the forward portion of the nose and creates higher heating
rates over the portion of the nose near the nose-cylinder junction.
The latter effect may be due to the shear layer created by the shock
impinging on the surface. Also this effect seems to lessen as the spike
length is increased and the impingement point of the shock moves aft.
On the afterbody the spike appears to cause an effect on heating rates
similar to that occurring on the pressure levels over the nose. First,
there is a decrease in the heating rate from an l/d of 0.5 to 1.0
followed by an increase in the local heating rate.

In general the effect of the spike on the hemisphere-cylinder is
to lower the overall heat transfer to the body. The maximum reductions
for increasing spike length occur for values of l/d from 0.5 to 3.0.
For an l/d greater than 3, the effect of increasing the spike is
negligible in lowering the heating rate. However, it should be noted
that for values of l/d of 3 or greater the integrated heat transfer
to the surface is approximately 65 percent lower than the $l/d = 0$ value.
It is interesting to note also that although the n = 2 model (a
parabolic nose shape) gives lower attainable drag, the hemisphere-cylinder
will give lower local heating rates.

L
1
3
4
5

CONCLUSIONS

On the basis of the results of the present investigation the following conclusions can be made:

1. The pressure distributions on the nose shapes investigated were found to be well predicted by either the conical flow theory or the matched Newtonian-Prandtl-Meyer expansion except near the nose-cylinder junction where boundary-layer bleedoff effects appeared to be present. On the cylindrical afterbodies the modified blast-wave theory adequately predicts pressure distributions with the exception of the hemisphere-cylinder for which viscous effects must be included.

2. The results of previous pressure distribution and heat-transfer investigations of spiked-nose-blunt bodies were seen to prevail at the higher Mach number of the present investigation.

3. The heat transfer on a 26.62° cone was found to be well predicted by a modification of Lees' theory to account for the variation of the product of the density and viscosity.

4. Lees' method of predicting the heat-transfer distribution on blunt bodies shows good agreement with the data obtained in this investigation. The modification of Lees' theory to allow for the variation of the product of the density and the coefficient of viscosity gave only slightly different results than the unmodified theory.

5. Although lower heating rates are obtainable on the spike-nosed hemisphere, the parabolic nose shape equipped with a flow-separation spike gives lower pressure drag than the spike-nosed hemisphere.

Langley Research Center,
　　National Aeronautics and Space Administration,
　　　　Langley Field, Va., April 3, 1961.

L
1
3
4
5

REFERENCES

1. Allen, H. Julian, and Eggers, A. J., Jr.: A Study of the Motion and Aerodynamic Heating of Ballistic Missiles Entering the Earth's Atmosphere at High Supersonic Speeds. NACA Rep. 1381, 1958. (Supersedes NACA TN 4047.)

2. Crawford, Davis H.: Investigation of the Flow Over a Spiked-Nose Hemisphere-Cylinder at a Mach Number of 6.8. NASA TN D-118, 1959.

3. Moeckel, W. E.: Flow Separation Ahead of Blunt Bodies at Supersonic Speeds. NACA TN 2418, 1951.

4. Stalder, Jackson R., and Nielsen, Helmer V.: Heat Transfer From a Hemisphere-Cylinder Equipped With Flow-Separation Spikes. NACA TN 3287, 1954.

5. Bogdonoff, Seymour M., and Vas, Irwin E.: Preliminary Investigation of Spiked Bodies at Hypersonic Speeds. Jour. Aero/Space Sci., vol. 26, no. 2, Feb. 1959, pp. 65-74.

6. Chapman, Dean R., Kuehn, Donald M., and Larson, Howard K.: Preliminary Report on a Study of Separated Flows in Supersonic and Subsonic Streams. NACA RM A55L14, 1956.

7. Henderson, Arthur, Jr.: Investigation of the Flow Over Simple Bodies at Mach Numbers of the Order of 20. NASA TN D-449, 1960.

8. Ferri, Antonio: A Review of Some Recent Developments in Hypersonic Flow. WADC Tech. Note 58-230, ASTIA Doc. No. AD 155 822, U.S. Air Force, Sept. 1958.

9. Henderson, Arthur, Jr., and Johnston, Patrick J.: Fluid-Dynamic Properties of Some Simple Sharp- and Blunt-Nosed Shapes at Mach Numbers From 16 to 24 in Helium Flow. NASA MEMO 5-8-59L, 1959.

10. Henderson, Arthur, Jr., and Swalley, Frank E.: Effects of Air Contamination in a Helium Tunnel. NASA TN D-406, 1960.

11. Erickson, Wayne D.: Real-Gas Correction Factors for Hypersonic Flow Parameters in Helium. NASA TN D-462, 1960.

12. Cooper, Morton, and Mayo, Edward E.: Measurements of Local Heat Transfer and Pressure on Six 2-Inch-Diameter Blunt Bodies at a Mach Number of 4.95 and at Reynolds Numbers Per Foot Up to 81×10^6. NASA MEMO 1-3-59L, 1959.

L
1
3
4
5

13. Lucks, C. F., Bing, G. F., Matolich, J., Deem, H. W., and Thompson, H. B.: The Experimental Measurement of Thermal Conductivities, Specific Heats, and Densities of Metallic, Transparent, and Protective Materials - Part II. AF Tech. Rep. No. 6145 (Contract No. AF 33(038)-20558), June 1, 1955.

14. Goldsmith, Alexander, and Waterman, Thomas E.: Thermophysical Properties of Solid Materials. WADC Tech. Rep. 58-476, ASTIA Doc. No. 207905, U.S. Air Force, Jan. 1959.

15. Lees, Lester, and Kubota, Toshi: Inviscid Hypersonic Flow Over Blunt-Nosed Slender Bodies. Jour. Aero. Sci., vol. 24, no. 3, Mar. 1957, pp. 195-202.

16. Love, E. S.: Prediction of Inviscid Induced Pressures From Round Leading Edge Blunting at Hypersonic Speeds. ARS Jour. (Tech. Notes), vol. 29, no. 10, pt. 1, Oct. 1959, pp. 792-794.

17. Wagner, Richard D., Jr.: Some Aspects of the Modified Newtonian and Prandtl-Meyer-Expansion Method for Axisymmetric Blunt Bodies at Zero Angle of Attack. Jour. Aero/Space Sci. (Reader's Forum), vol. 26, no. 12, Dec. 1959, pp. 851-852.

18. Mueller, James N., Close, William H., and Henderson, Arthur, Jr.: An Investigation of Induced-Pressure Phenomena on Axially Symmetric, Flow-Alined, Cylindrical Models Equipped With Different Nose Shapes at Free-Stream Mach Numbers From 15.6 to 21 in Helium. NASA TN D-373, 1960.

19. Lees, Lester: Laminar Heat Transfer Over Blunt-Nosed Bodies at Hypersonic Flight Speeds. Jet Propulsion, vol. 26, no. 4, Apr. 1956, pp. 259-269, 274.

20. Stine, Howard A., and Wanlass, Kent: Theoretical and Experimental Investigation of Aerodynamic-Heating and Isothermal Heat-Transfer Parameters on a Hemispherical Nose With Laminar Boundary Layer at Supersonic Mach Numbers. NACA TN 3344, 1954.

21. Kemp, Nelson H., Rose, Peter H., and Detra, Ralph W.: Laminar Heat Transfer Around Blunt Bodies in Dissociated Air. Jour. Aero/Space Sci., vol. 26, no. 7, July 1959, pp. 421-430.
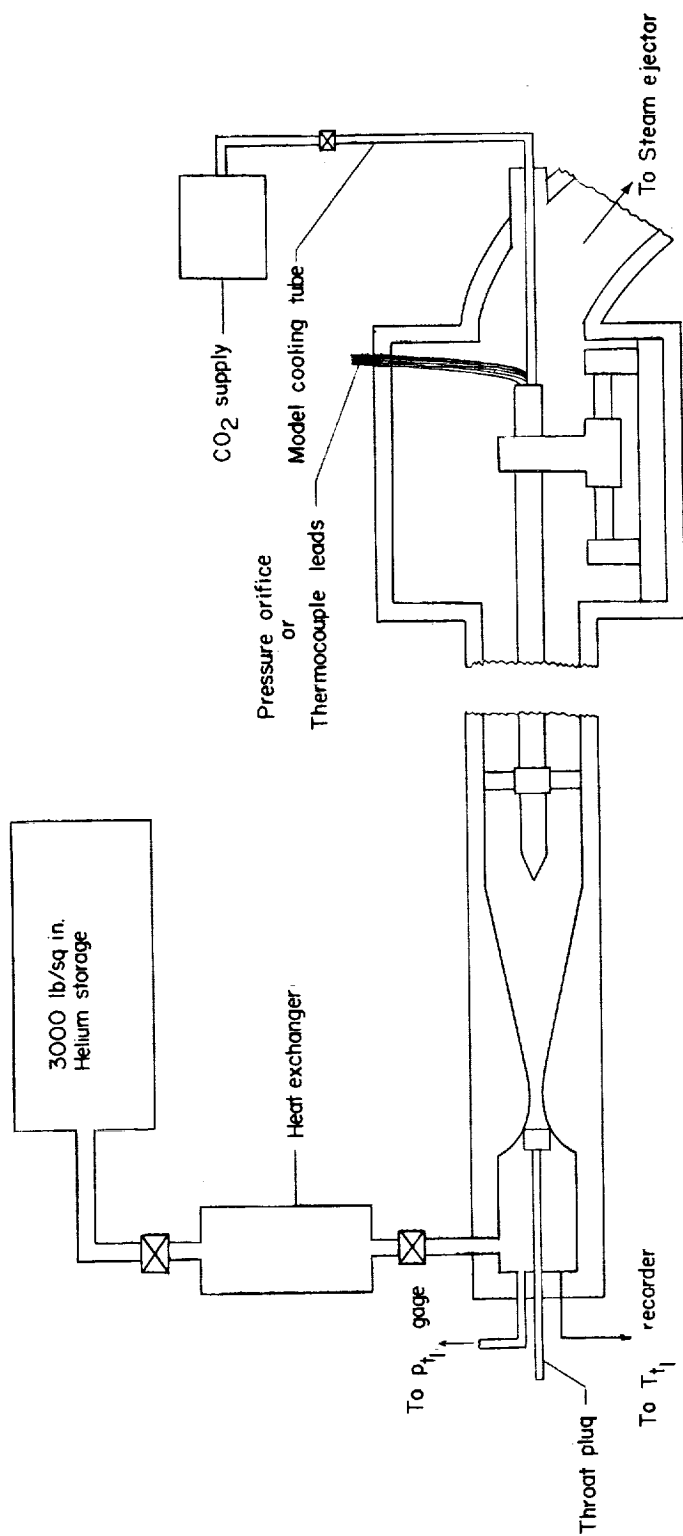
L
1
3
4
5

3000 lb/sq in.
Helium storage

Heat exchanger

To p_{t_1} gage

Throat plug

To T_{t_1} recorder

CO_2 supply

Pressure orifice
or
Thermocouple leads

Model cooling tube

To Steam ejector

Figure 1.- Schematic diagram of tunnel and test apparatus.

Pressure Orifices	Thermocouples	
	$\tau = 0.030$	$\tau = 0.010$
s/b	s/b	s/b
0.232	0.232	0.232
.365	.365	.365
.499	.499	.499
.699	.699	.699
.899	.899	.899
1.088	1.088	1.088
1.356	1.356	1.356
1.715	1.715	1.715

Pressure Orifices	Thermocouples	
	$\tau = 0.030$	$\tau = 0.010$
s/b	s/b	s/b
0.169	0	0
.368	.169	.169
.559	.368	.368
.693	.559	.559
.923	.693	.693
1.100	.923	.923
1.360	1.100	1.100
1.710	1.360	1.360
	1.710	1.710

Pressure Orifices	Thermocouples	
	$\tau = 0.030$	$\tau = 0.010$
s/b	s/b	s/b
0.129	0.129	0
.256	.256	.129
.348	.348	.256
.516	.516	.348
.675	.675	.516
.911	.911	.675
1.075	1.075	.911
1.345	1.345	1.075
		1.345

Pressure Orifices	Thermocouples	
	$\tau = 0.030$	$\tau = 0.010$
s/b	s/b	s/b
0.122	0.122	0
.202	.202	.122
.248	.248	.180
.291	.291	.2345
.453	.453	.291
.767	.767	.453
1.078	1.078	.767
1.465	1.465	1.078
		1.455

Pressure Orifices	Thermocouples	
	$\tau = 0.030$	$\tau = 0.010$
s/b	s/b	s/b
0.103	0.103	0
.155	.155	.103
.216	.216	.155
.260	.260	.216
.315	.315	.260
.630	.630	.315
.925	.925	.630
1.076	1.076	.925
		1.076

Pressure Orifices	Thermocouples	
	$\tau = 0.030$	$\tau = 0.010$
s/b	s/b	s/b
0.167	0.167	0
.333	.333	.130
.500	.500	.196
.667	.667	.319
.833	.833	.428
1.0373	1.266	.502
1.588	1.650	.537
2.150	2.150	.608

Figure 2.- Drawings of models with pressure orifice and thermocouple locations.

Pressure orifices
or
thermocouples

45°

0.375

0.375

1.0

0.375

0.030

Cooling tube

Spike tube

(a) Sets one and two.

Bulkhead

Spike tube

Cooling tube

Thermocouples

Coolant exits

Thermocouples

45°

0.375

2.50

0.375

0.25°

Bulkhead

0.010

Cooling tube

Spike tube
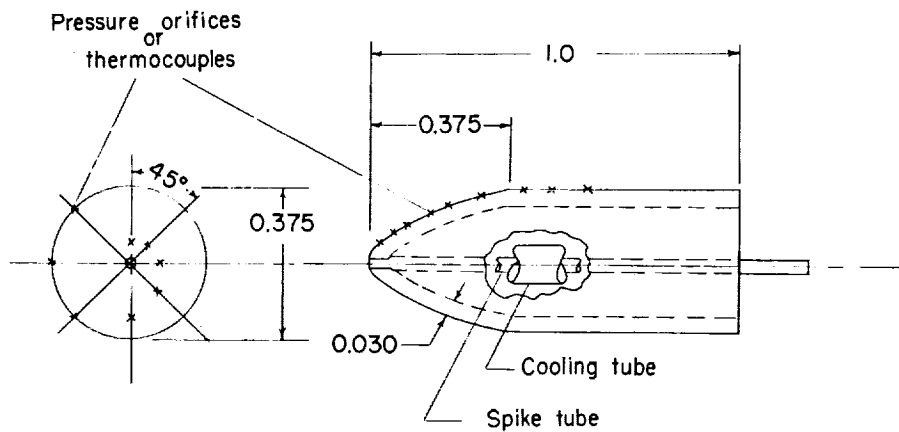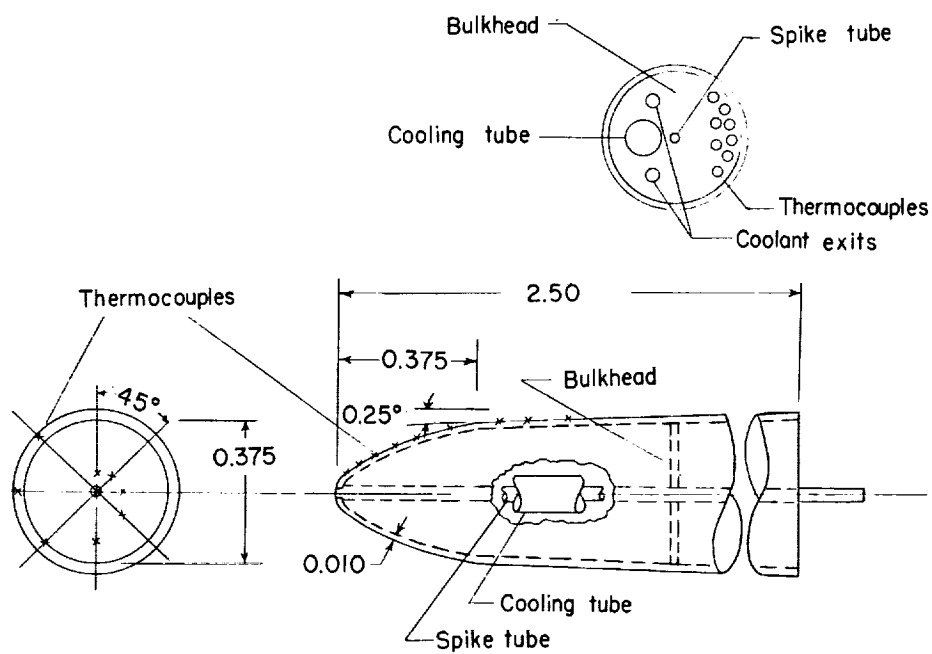
(b) Set three.

Figure 3.- Typical construction of models.

L-1345

L-1345

Model support

Wires attached to
pneumatic cylinder

Copper bushings

Micarta sleeve

Test model

Paper disk
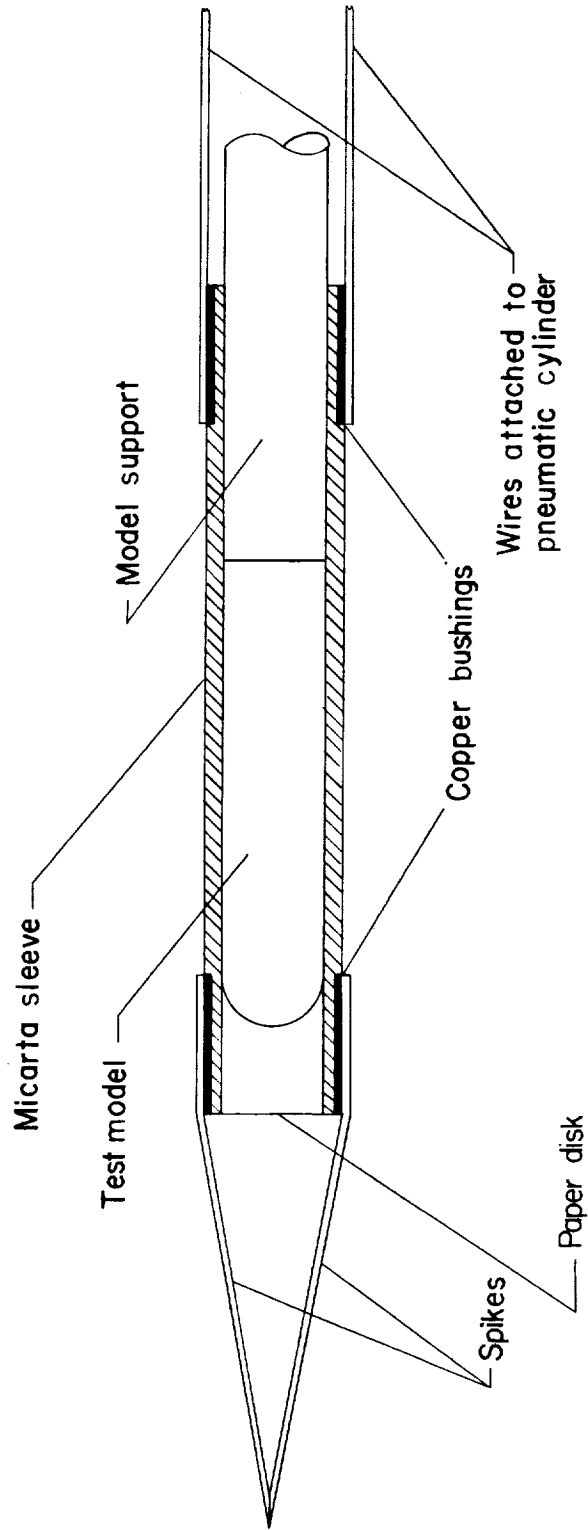
Spikes

Figure 4.- Model starting and insulating device.
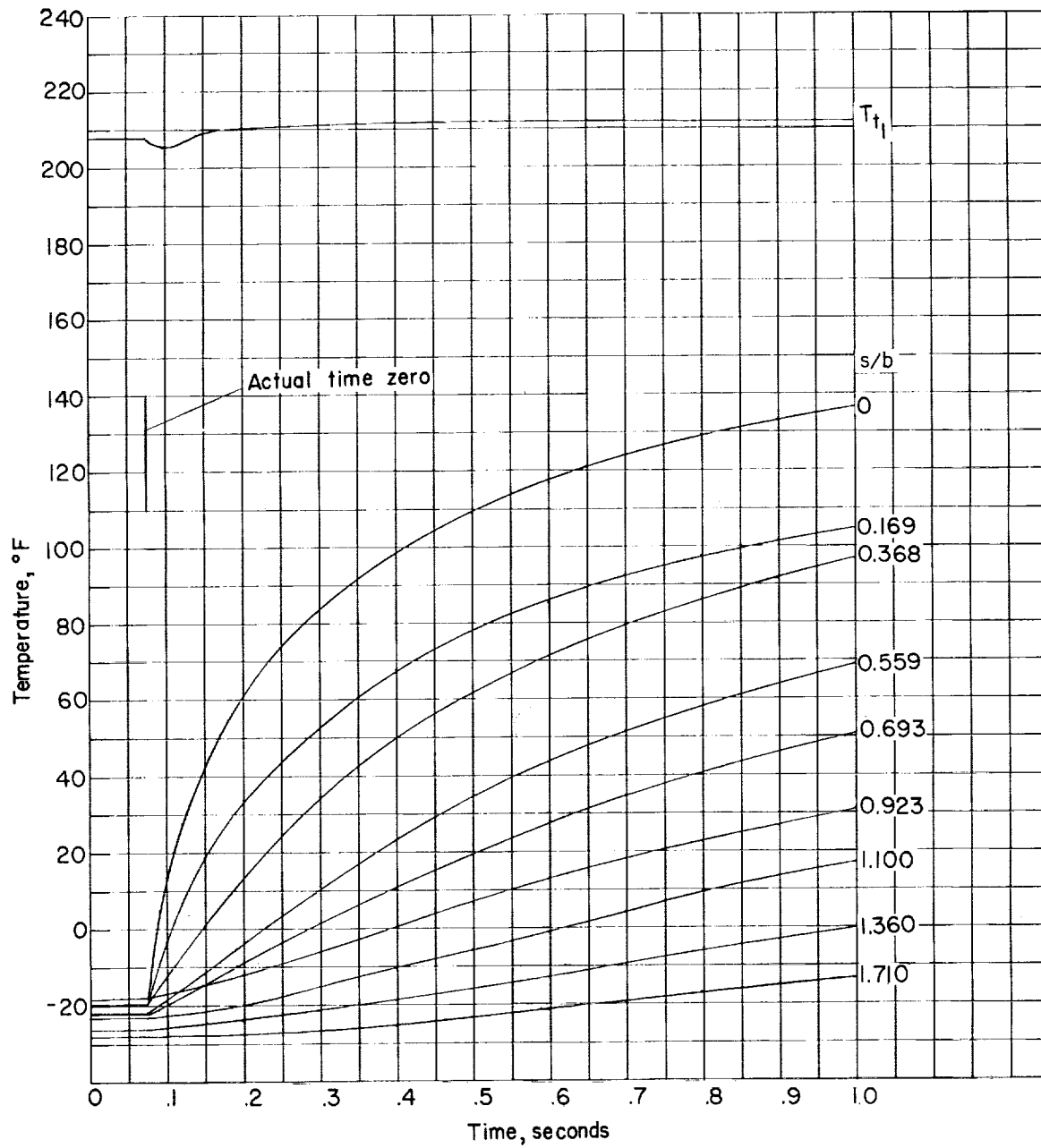
(a) n = 2 body using plug start.

Figure 5.- Temperature-time histories. τ = 0.010 inch.
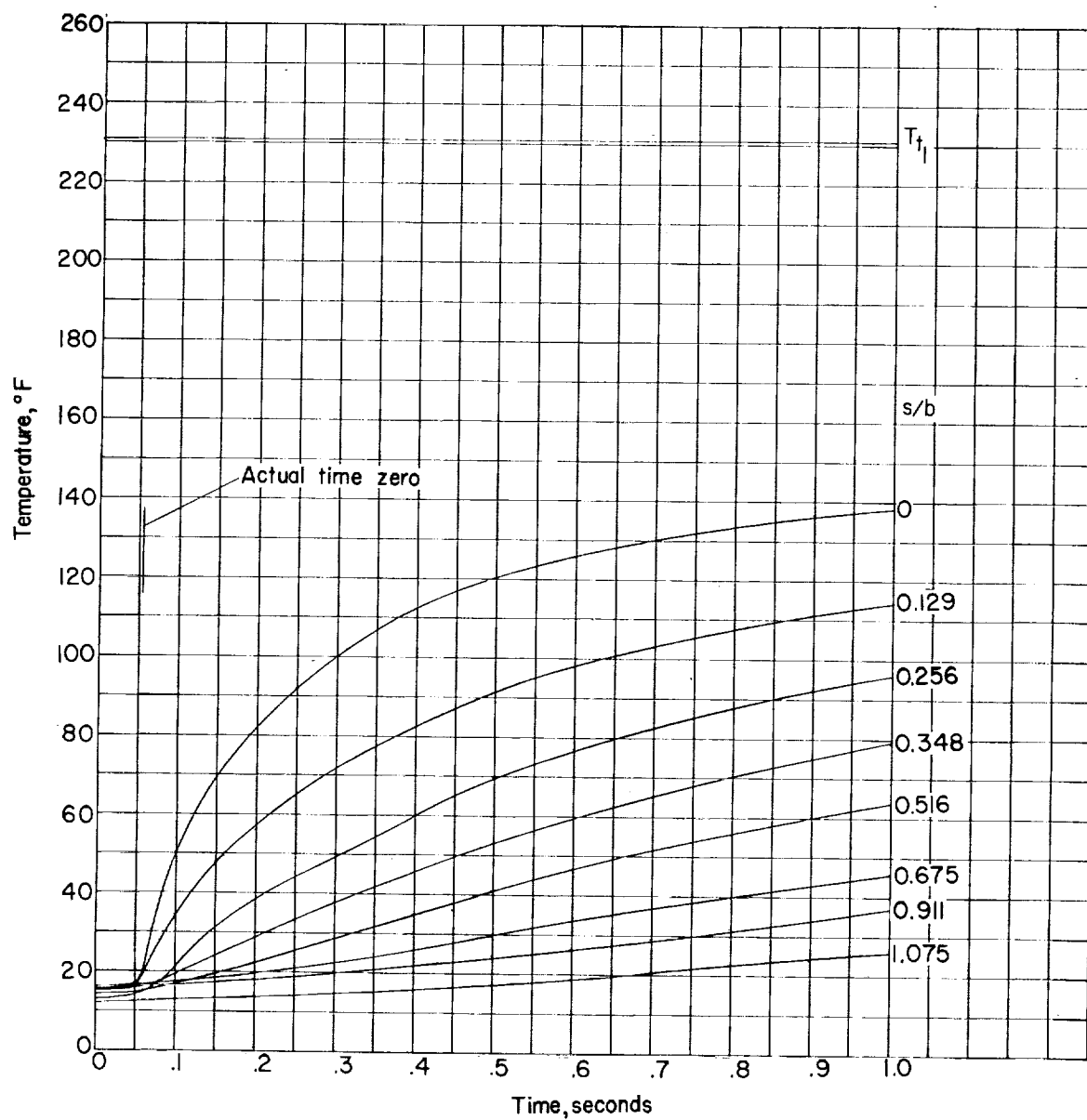
L-1345

(b) n = 4 body using sleeve start.

Figure 5.- Concluded.

n=1

n=6

←Scratch
in glass

n=2

n=8

n=4
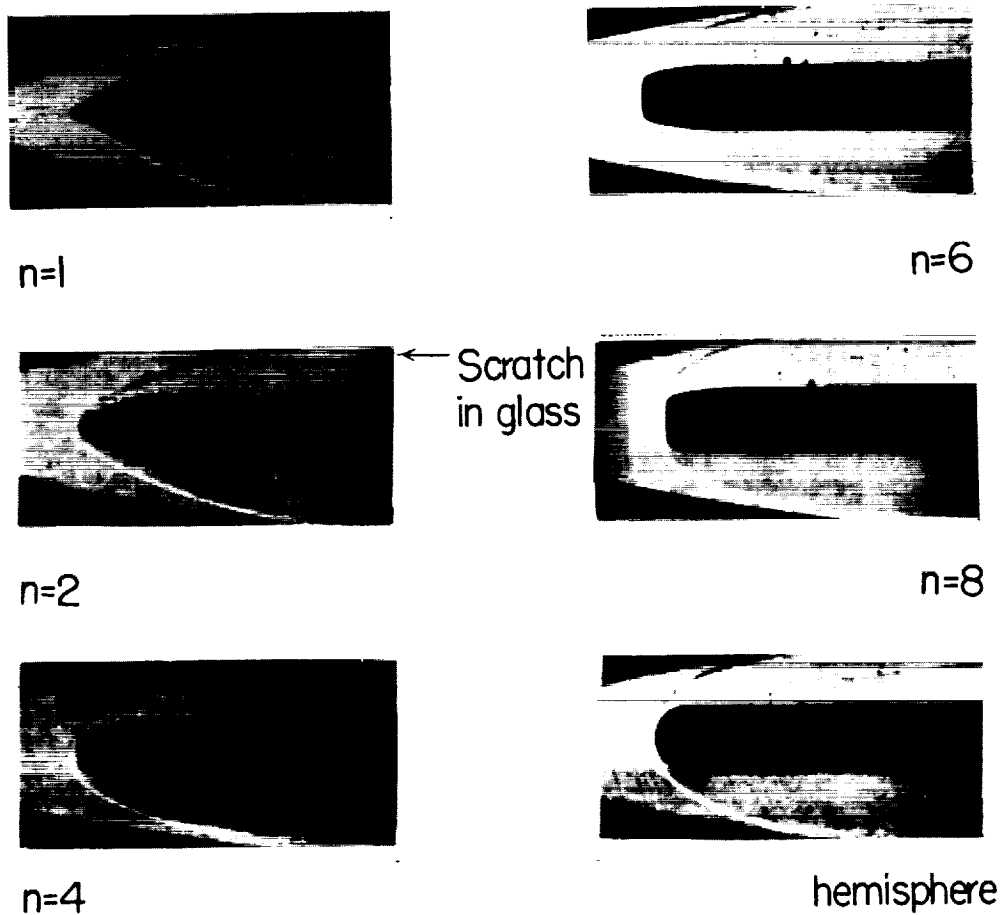
hemisphere

(a) Models without spikes. L-61-1084

Figure 6.- Schlieren photographs of models at M = 19.4 and
$R_d = 0.30 \times 10^6$.

L-1345

L-1345

$l/d=0$

$l/d=0.5$

$l/d=3$

$l/d=1$

$l/d=4$

$l/d=2$
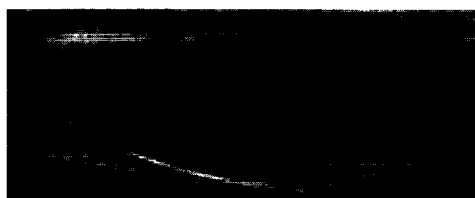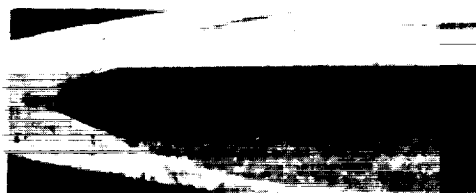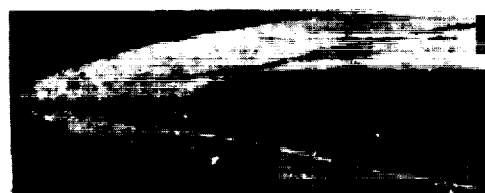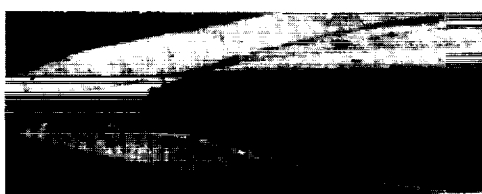
$l/d=4.59$

(b) n = 2 model with various spike lengths.   L-61-1085

Figure 6.- Continued.

$l/d=0$

$l/d=0.5$

$l/d=3$

$l/d=1$

$l/d=4$

$l/d=2$
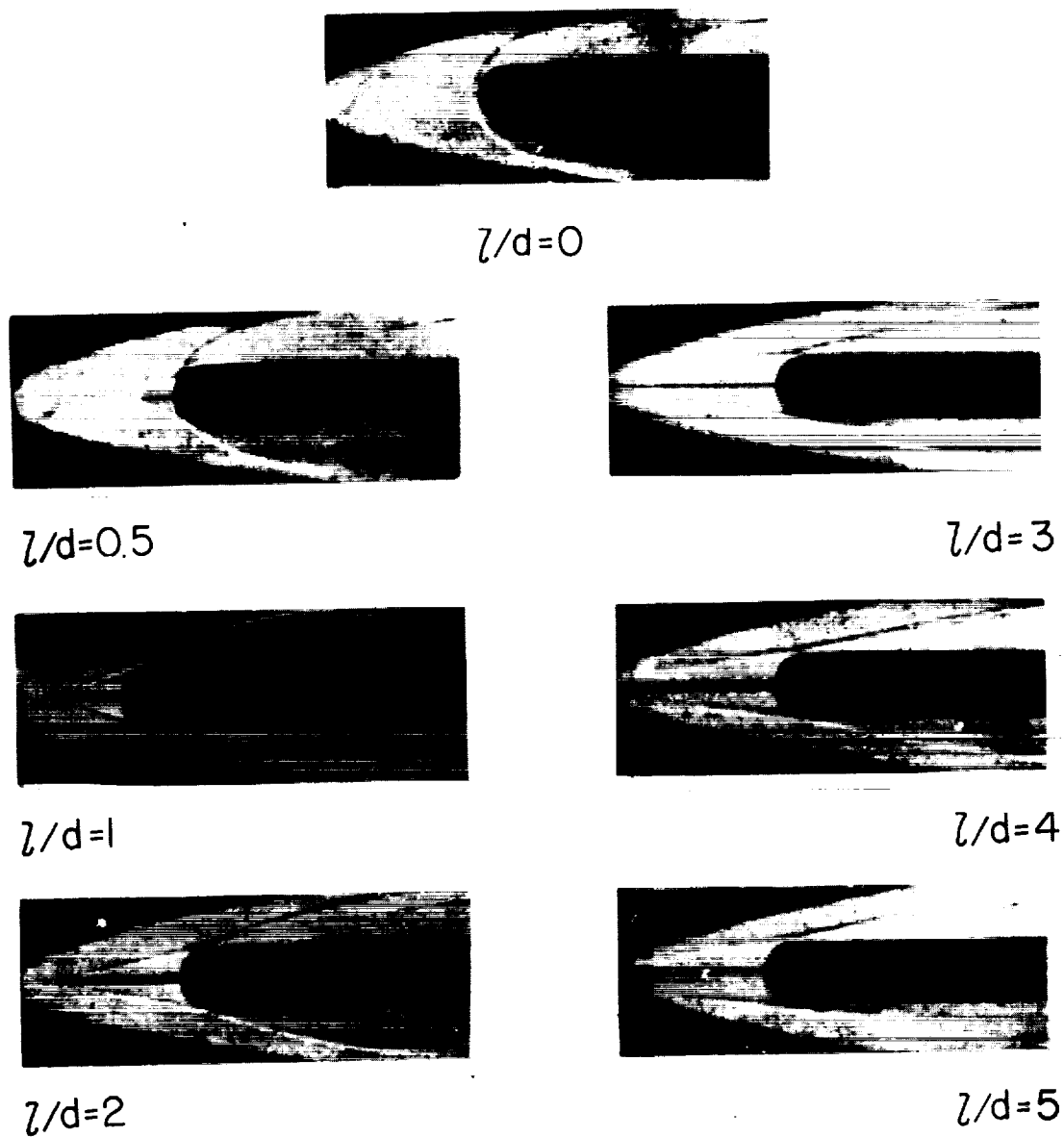
$l/d=5$

L-61-1086

(c) Hemisphere-cylinder model with various spike lengths.

Figure 6.- Concluded.
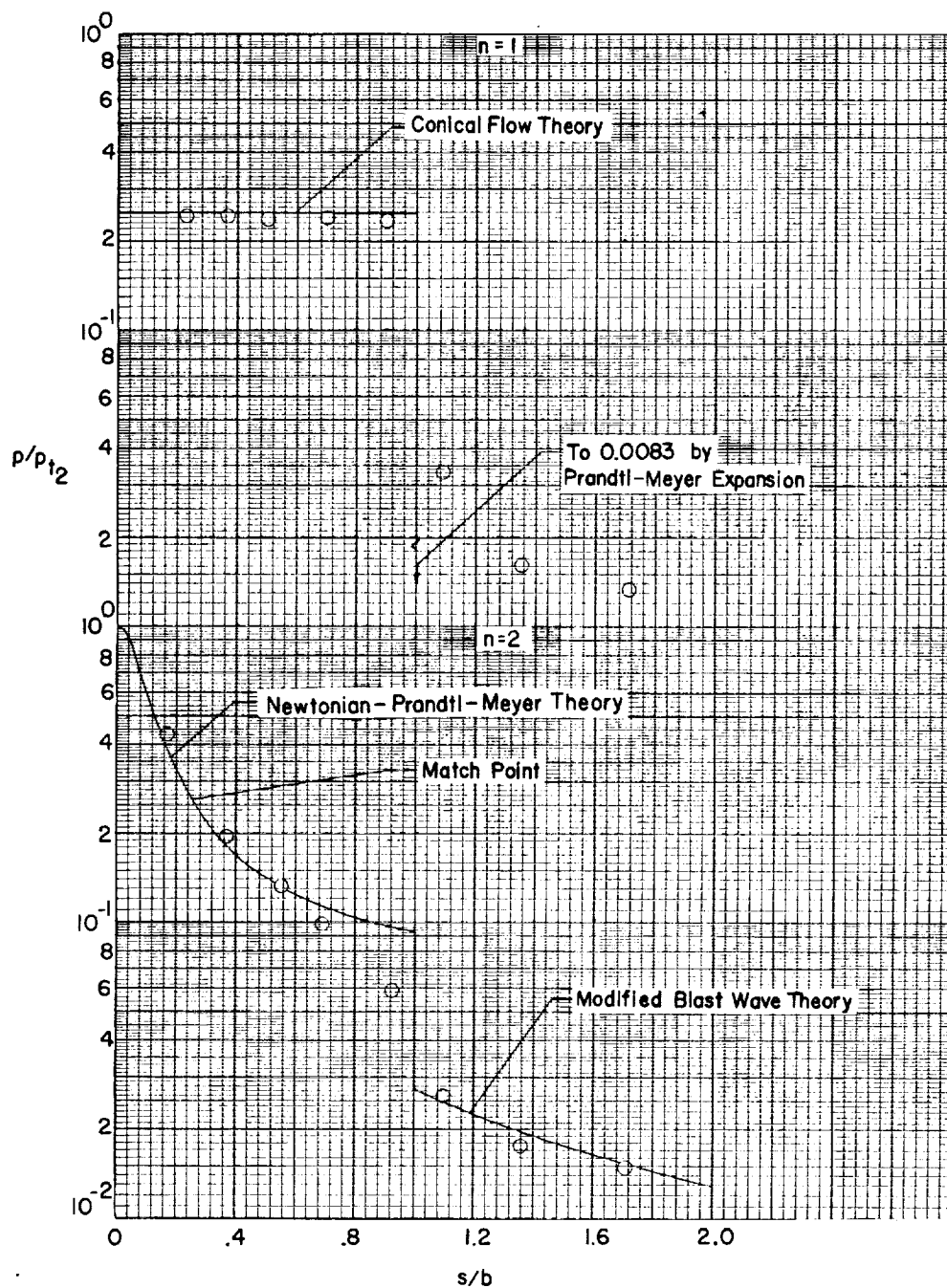
(a) n = 1 and n = 2 nose shapes.

Figure 7.- Pressure distributions on nose shapes at M = 19.4
and $R_d = 0.30 \times 10^6$.
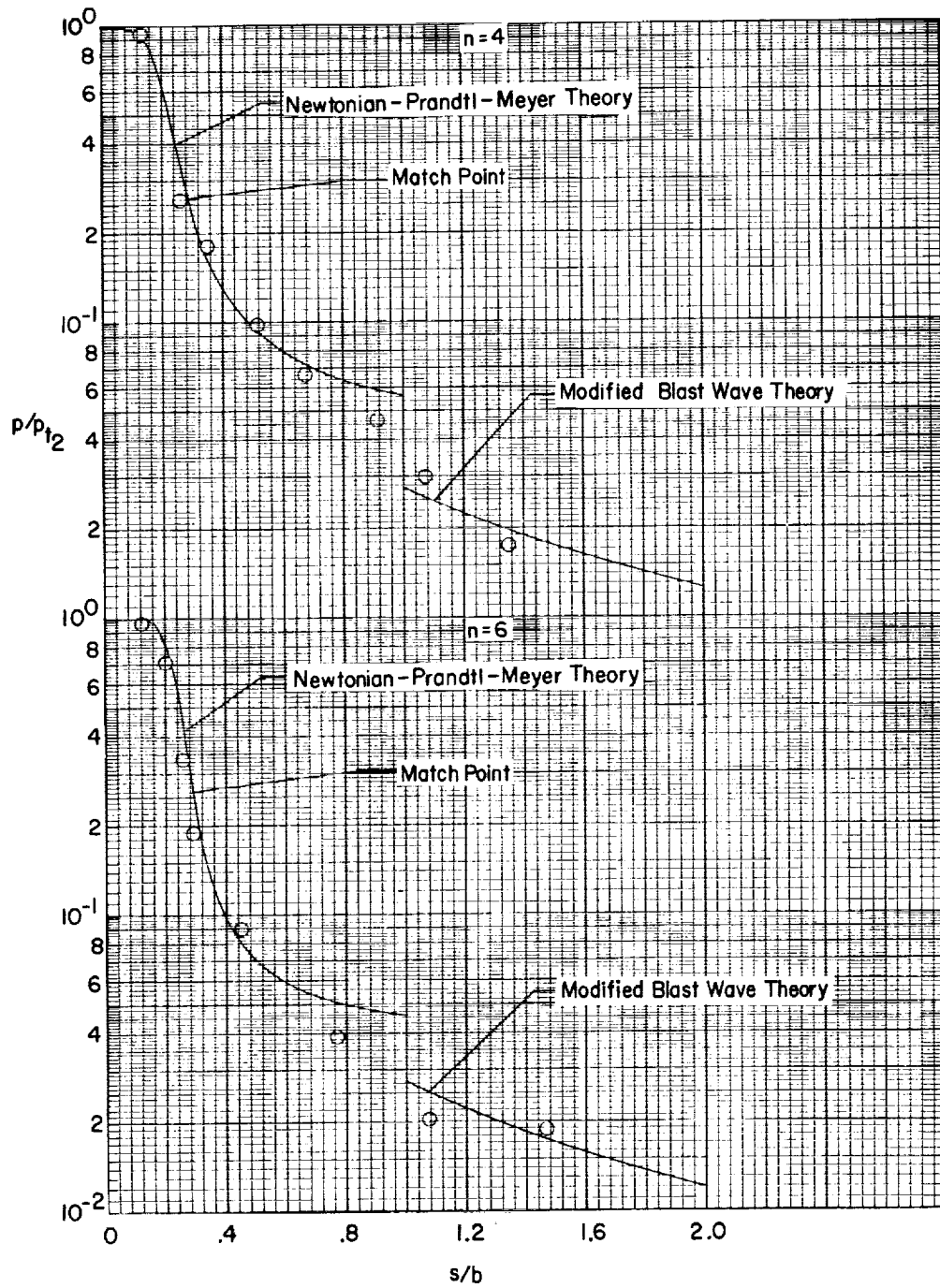
(b) n = 4 and n = 6 nose shapes.

Figure 7.- Continued.

L-1345
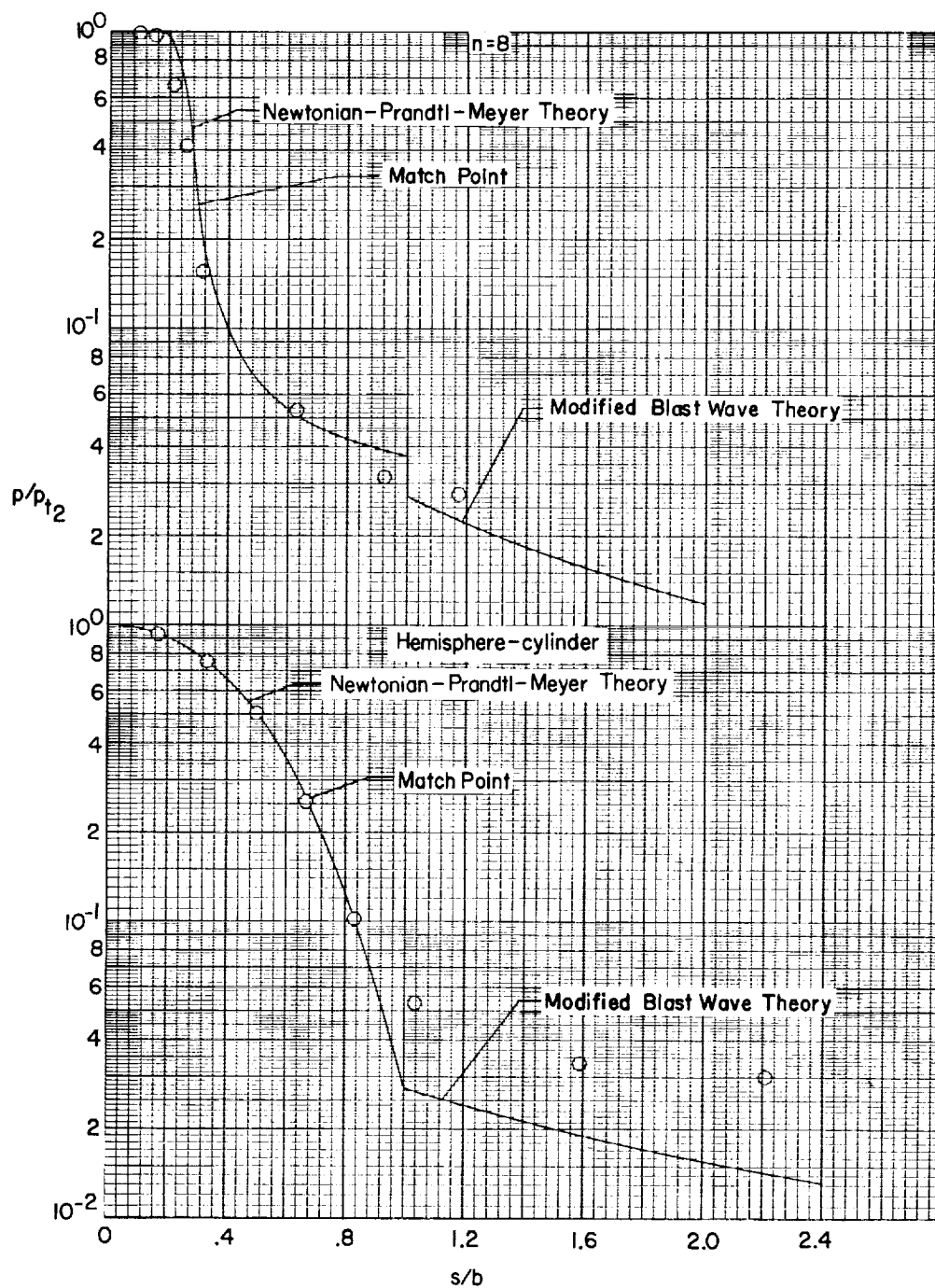
(c) n = 8 and hemisphere nose shapes.

Figure 7.- Concluded.
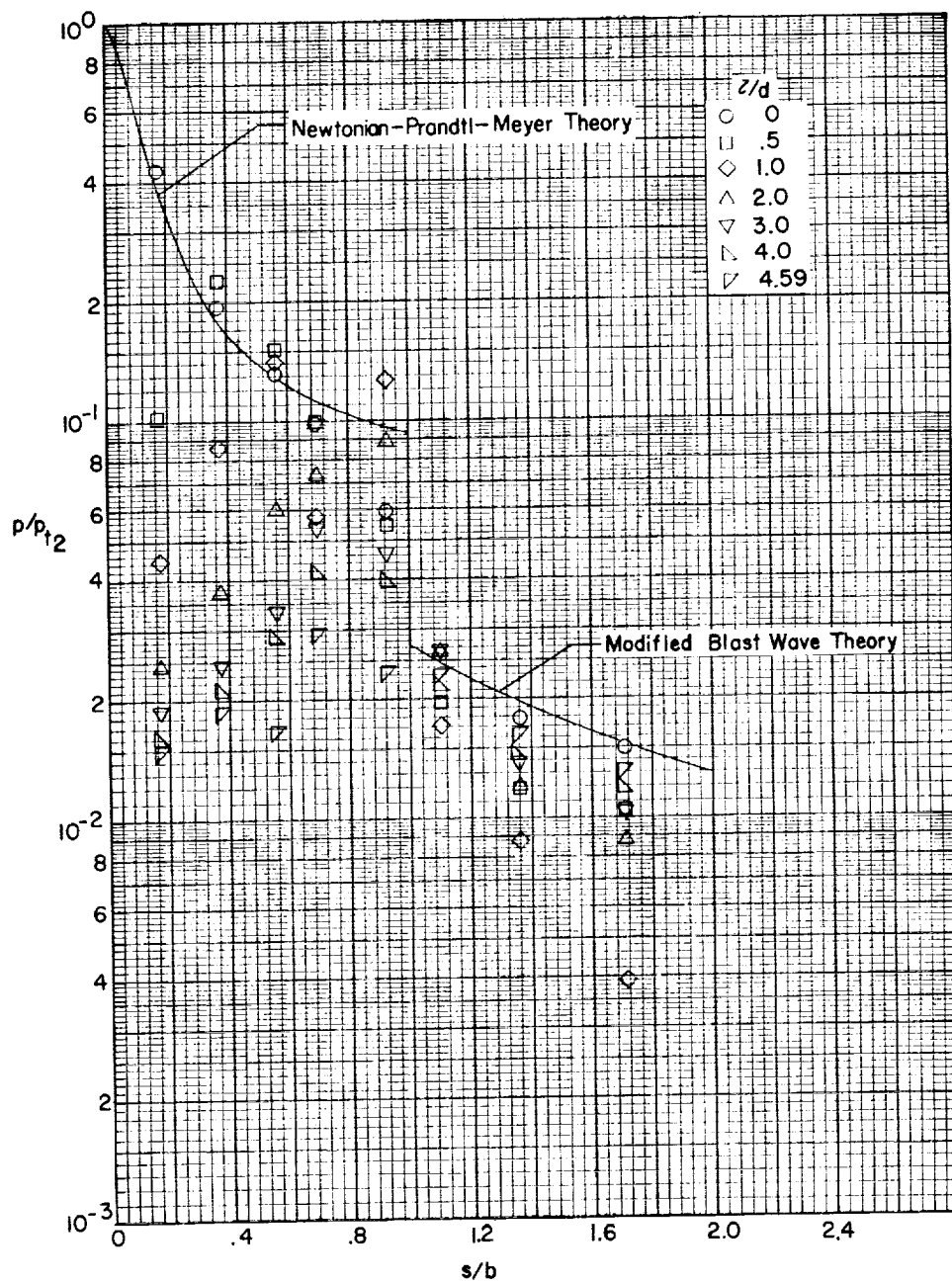
(a) n = 2 nose shape.

Figure 8.- Pressure distributions on spike nose shapes at M = 19.4
and R_d = 0.30 × 10^6.
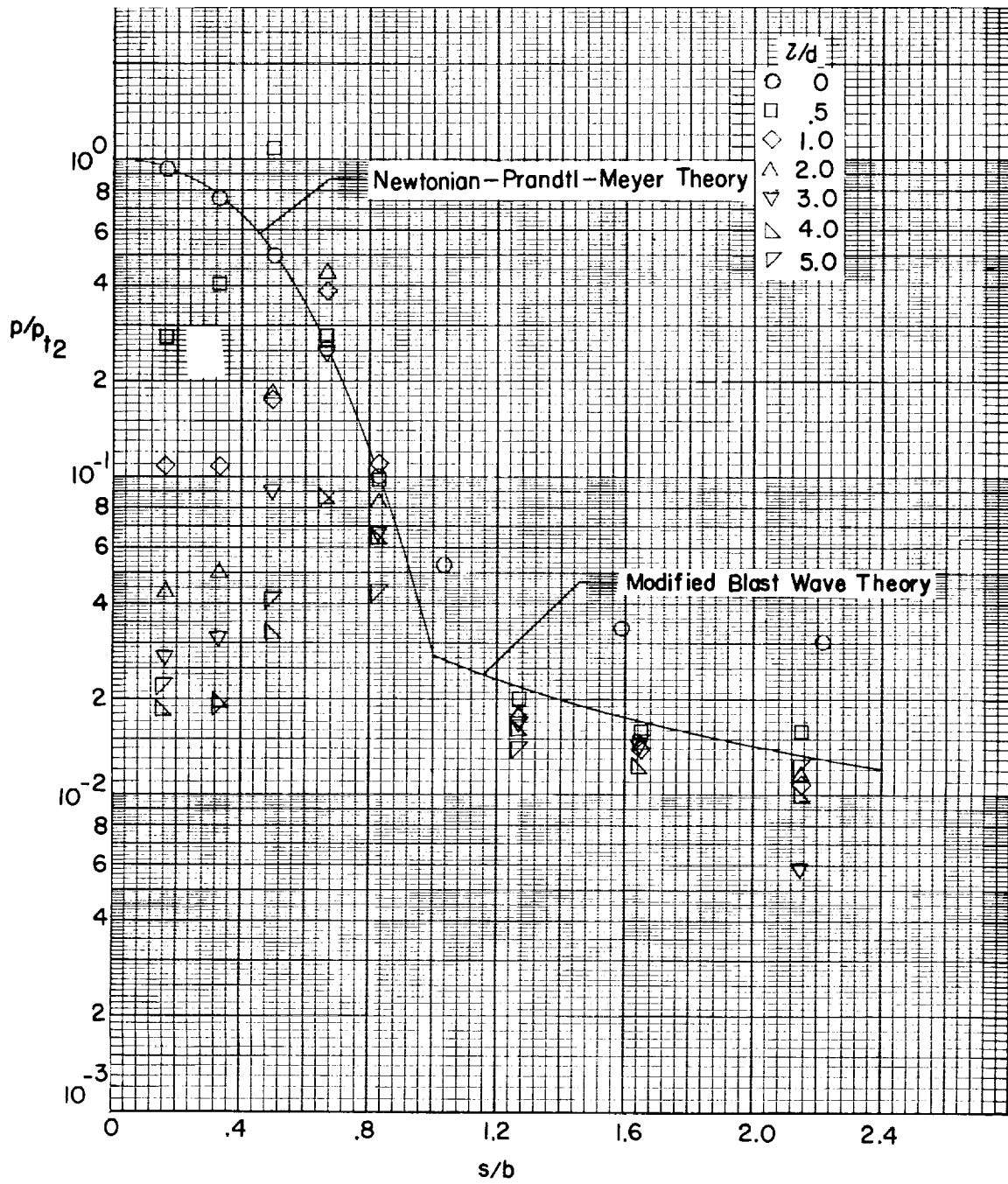
(b) Hemisphere-cylinder nose shape.

Figure 8.- Concluded.

(a) n = 2.

(b) Hemisphere-cylinder.
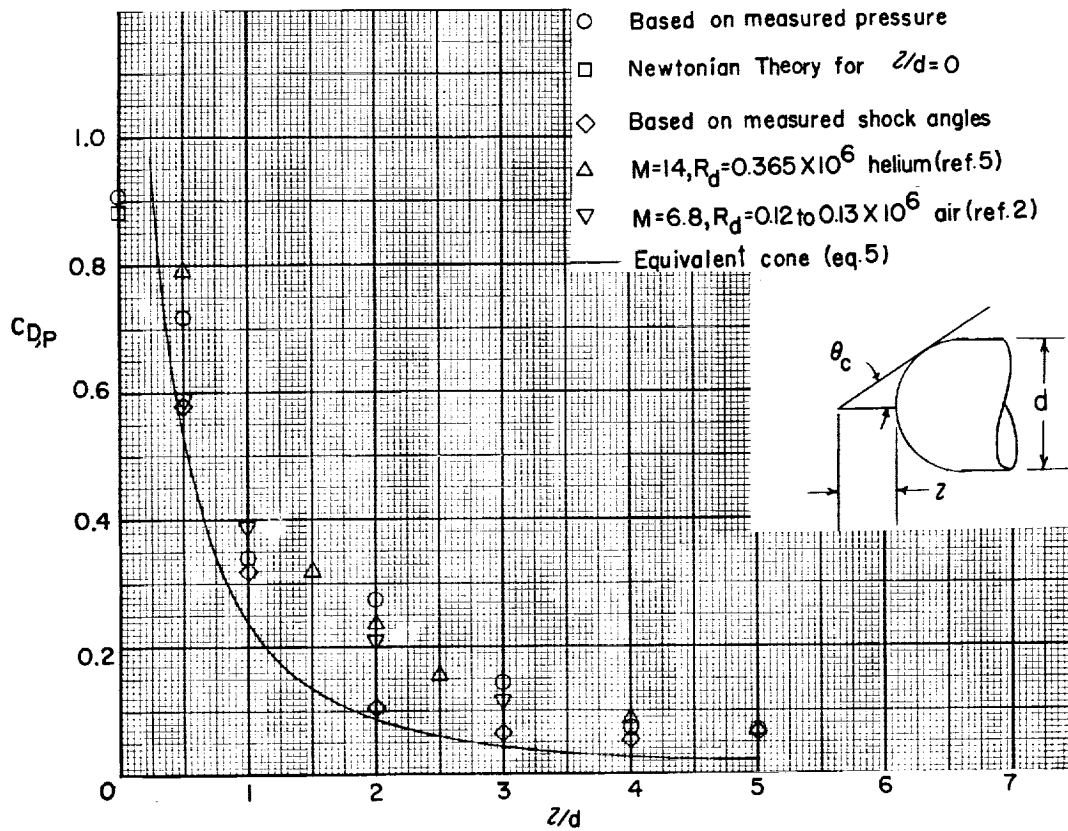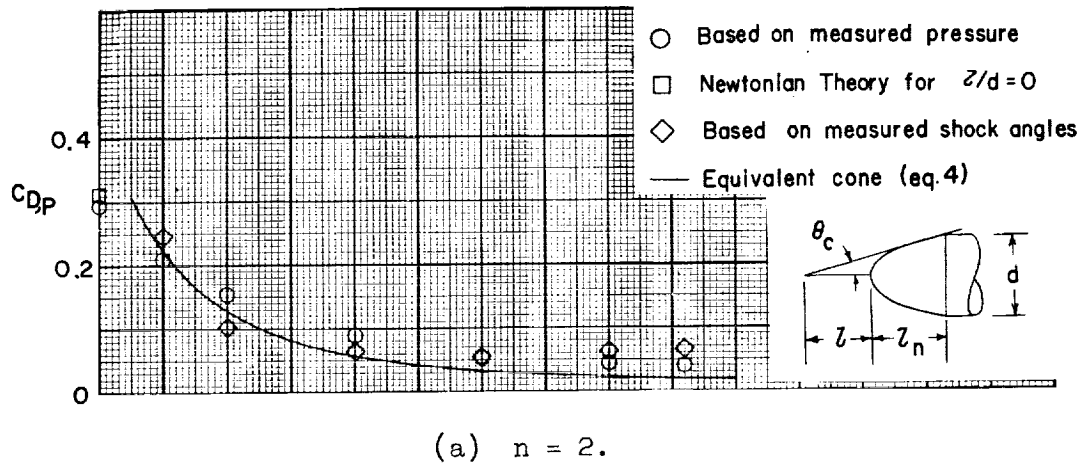
Figure 9.- Pressure drag coefficients of blunt nose shapes equipped with flow separation spikes.
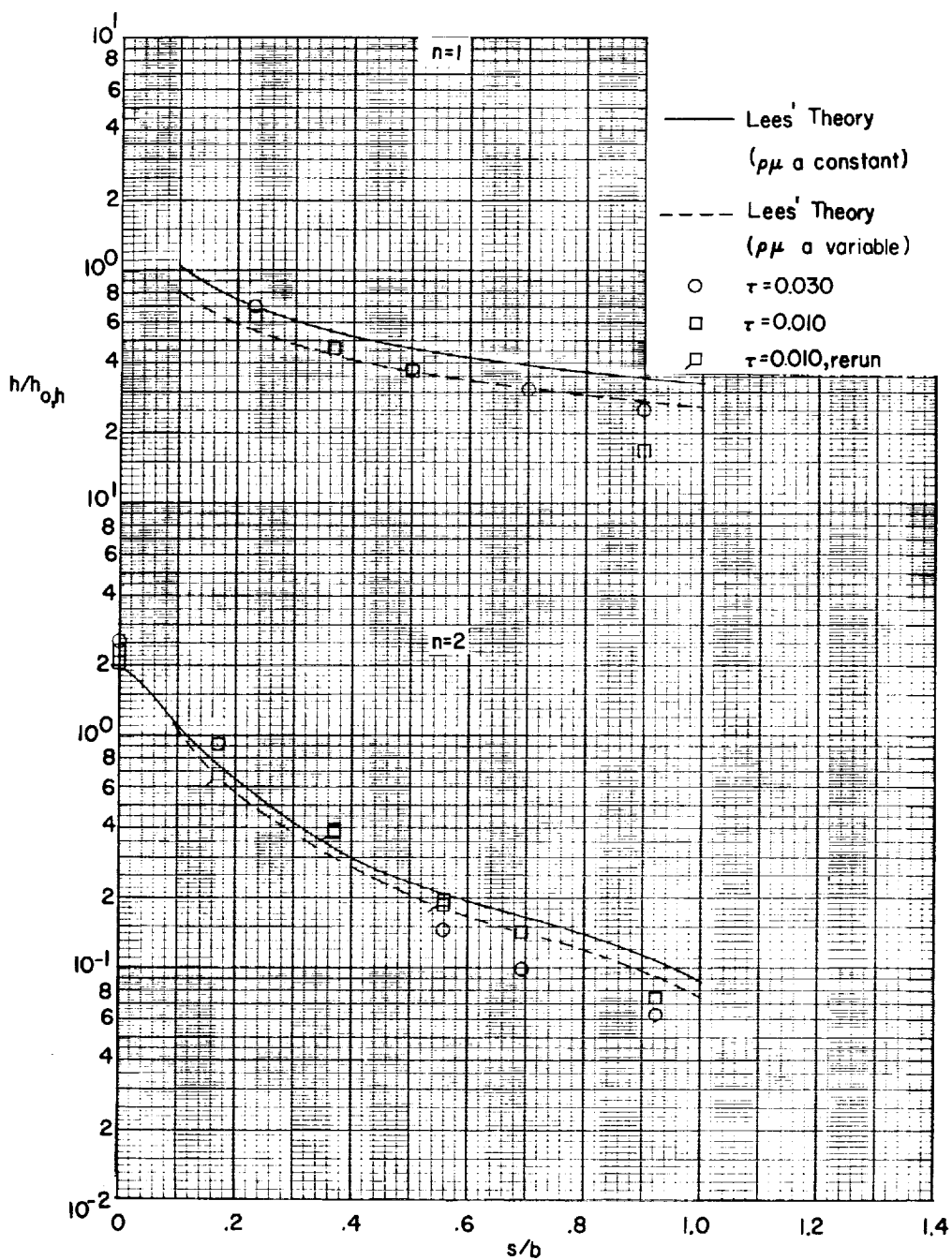
(a) n = 1 and n = 2 nose shapes.

Figure 10.- Heat transfer distributions on nose shapes at M = 19.4 and R_d = 0.23 × 10^6.
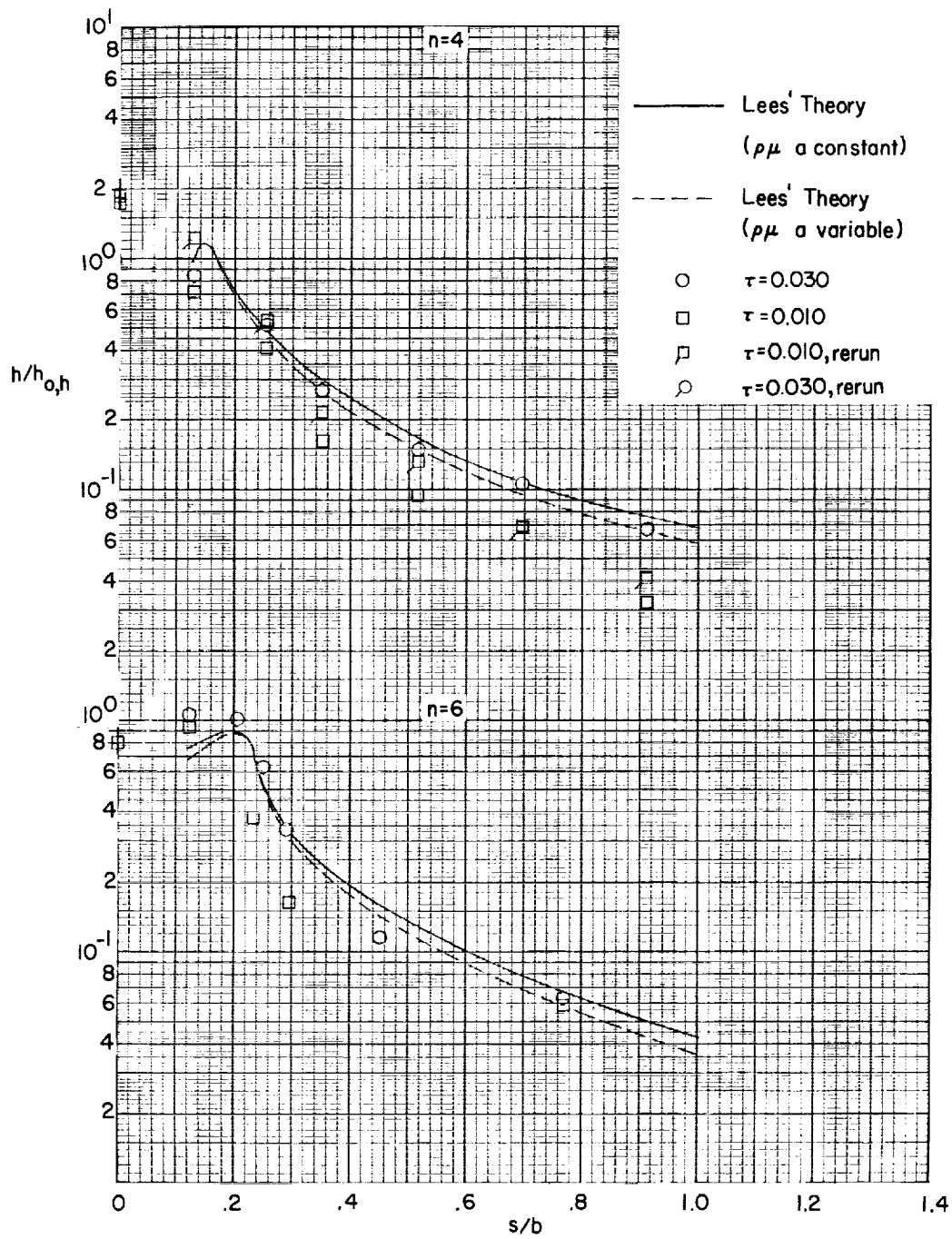
(b) n = 4 and n = 6 nose shapes.

Figure 10.- Continued.
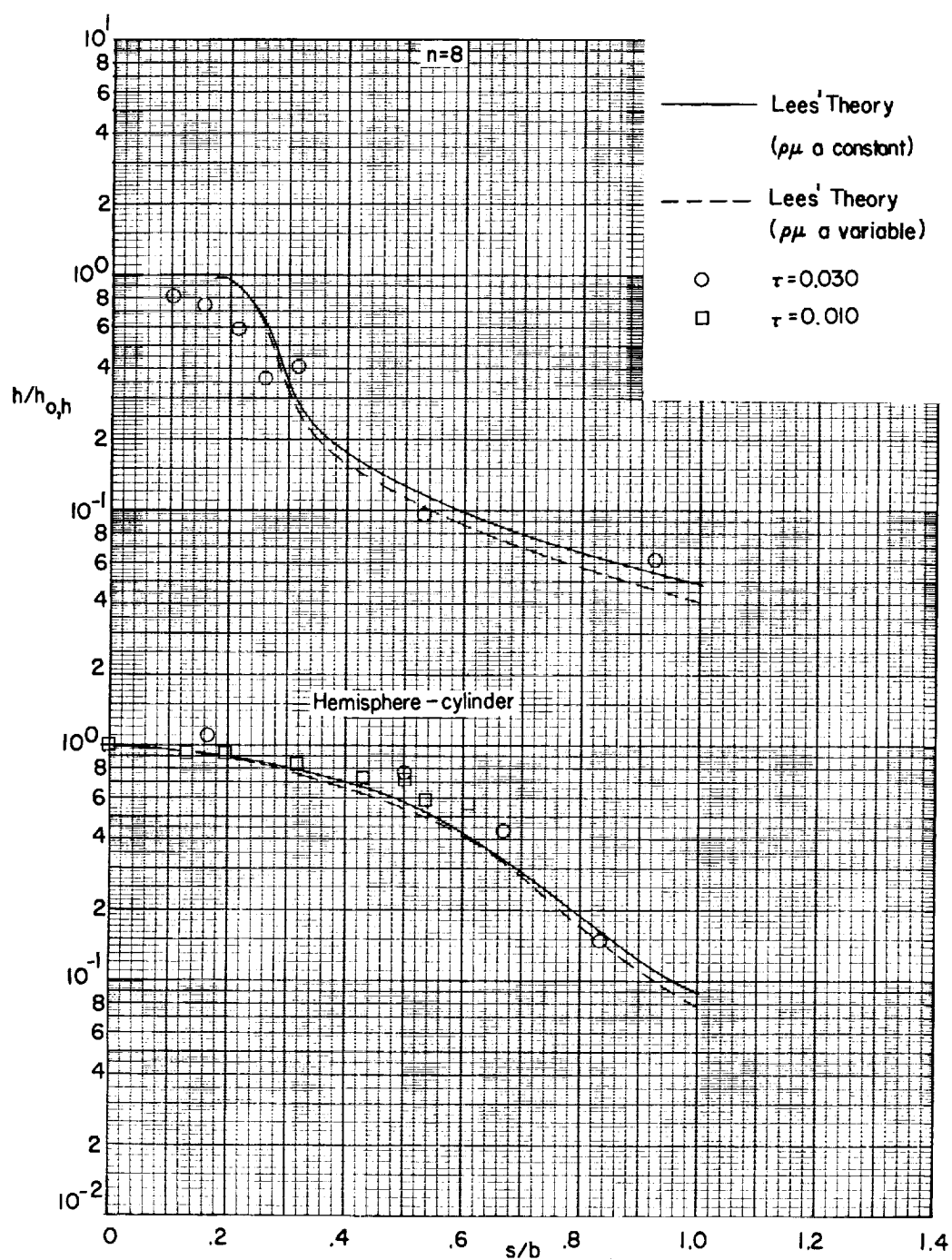
(c) n = 8 and hemisphere-cylinder nose shape.

Figure 10.- Concluded.
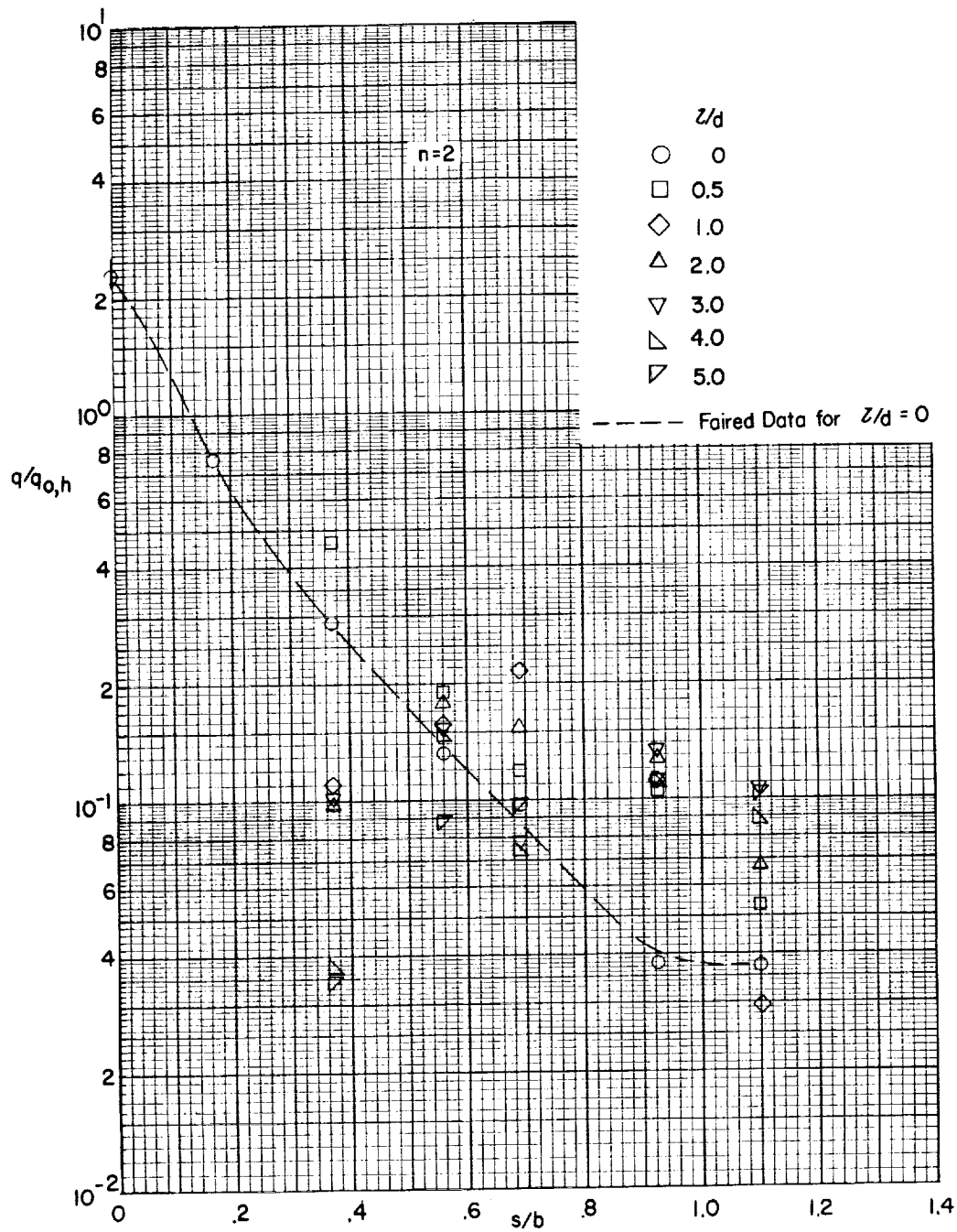
(a) n = 2 model.

Figure 11.- Heat-transfer distributions on spike-nose models at
M = 19.4 and $R_d = 0.23 \times 10^6$.
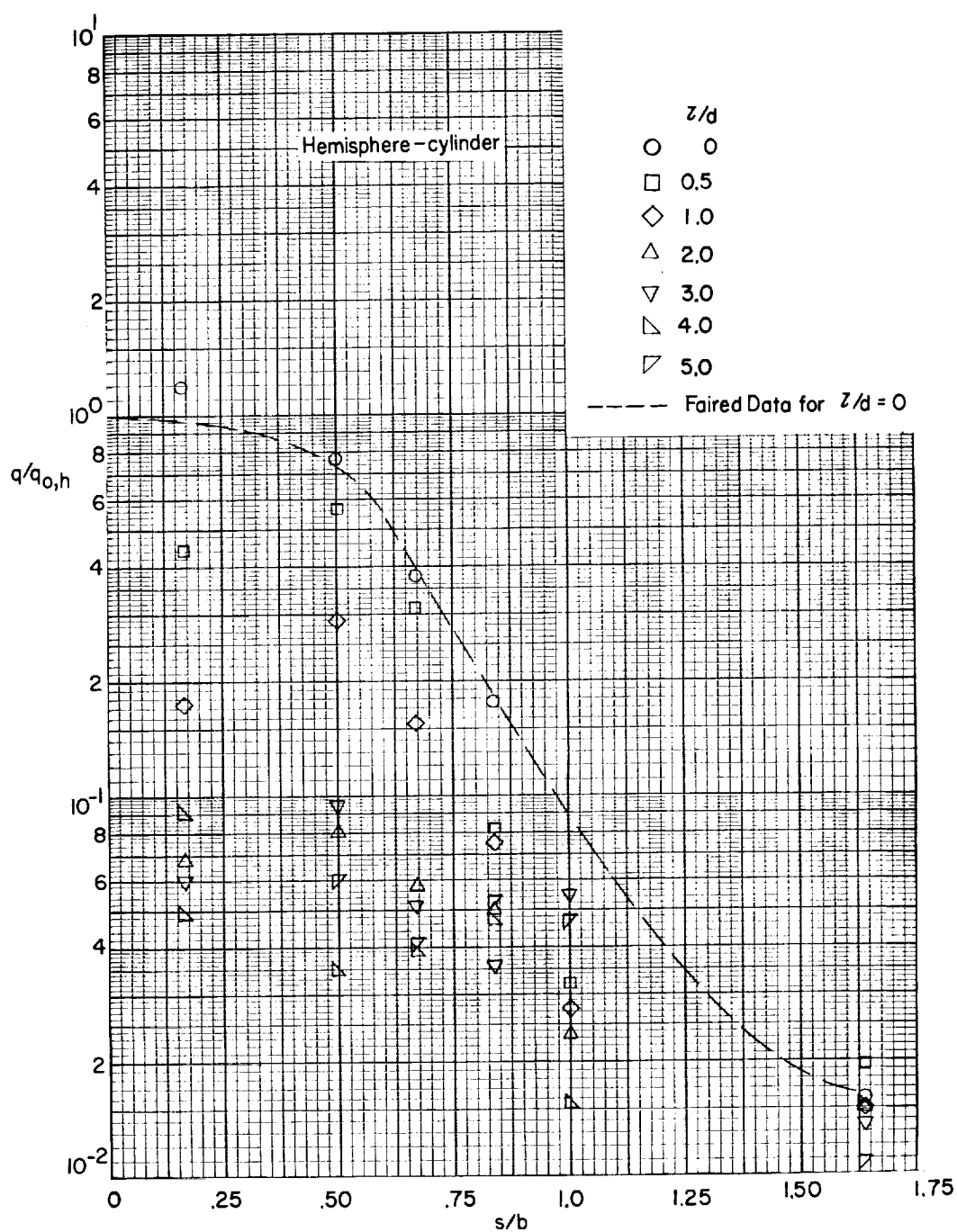
(b) Hemisphere-cylinder.

Figure 11.- Concluded.